LETTER

doi:10.1038/nature15754

Sublimation in bright spots on (1) Ceres

A. Nathues[1], M. Hoffmann[1], M. Schaefer[1], L. Le Corre[1,2], V. Reddy[1,2], T. Platz[1], E. A. Cloutis[3], U. Christensen[1], T. Kneissl[4], J.-Y. Li[2], K. Mengel[5], N. Schmedemann[4], T. Schaefer[1], C. T. Russell[6], D. M. Applin[3], D. L. Buczkowski[7], M. R. M. Izawa[3,8], H. U. Keller[9], D. P. O'Brien[2], C. M. Pieters[10], C. A. Raymond[11], J. Ripken[1], P. M. Schenk[12], B. E. Schmidt[13], H. Sierks[1], M. V. Sykes[2], G. S. Thangjam[1] & J.-B. Vincent[1]

The dwarf planet (1) Ceres, the largest object in the main asteroid belt[1] with a mean diameter of about 950 kilometres, is located at a mean distance from the Sun of about 2.8 astronomical units (one astronomical unit is the Earth–Sun distance). Thermal evolution models suggest that it is a differentiated body with potential geological activity[2,3]. Unlike on the icy satellites of Jupiter and Saturn, where tidal forces are responsible for spewing briny water into space, no tidal forces are acting on Ceres. In the absence of such forces, most objects in the main asteroid belt are expected to be geologically inert. The recent discovery[4] of water vapour absorption near Ceres and previous detection of bound water and OH near and on Ceres (refs 5–7) have raised interest in the possible presence of surface ice. Here we report the presence of localized bright areas on Ceres from an orbiting imager[8]. These unusual areas are consistent with hydrated magnesium sulfates mixed with dark background material, although other compositions are possible. Of particular interest is a bright pit on the floor of crater Occator that exhibits probable sublimation of water ice, producing haze clouds inside the crater that appear and disappear with a diurnal rhythm. Slow-moving condensed-ice or dust particles[9,10] may explain this haze. We conclude that Ceres must have accreted material from beyond the 'snow line'[11], which is the distance from the Sun at which water molecules condense.

We observed Ceres using the Framing Camera (FC) on board the Dawn spacecraft. The FC is equipped with a panchromatic (clear) filter and seven colour filters, covering the wavelength range 0.4 μm to 1.0 μm (ref. 8). Image calibration and spectral cube computation were performed as for the Vesta phase of the Dawn mission[12,13].

We find that the general surface of Ceres is rather dark (similar in brightness to fresh asphalt) and spotted with bright patches (ranging between the brightness of concrete and that of ocean ice). Figure 1 shows several bright spots across the surface. The inner part of the central spot on the floor of the Occator crater is the brightest surface on Ceres, with an absolute reflectance (converted from image reflectivity data by Hapke modelling) of ~0.25; the second-brightest feature (absolute reflectance ~0.07) is tentatively named feature A, and is associated with a 10-km-diameter crater far from Occator. We counted more than 130 bright spots on Ceres, most of them associated with impact craters (Extended Data Fig. 1).

The floor of Occator (diameter 90.5 km, depth 4 km) exhibits multiple, partially coalesced bright spots (Fig. 2a, Extended Data Figs 2 and 4). The largest of these spots corresponds to a central pit (~10 km wide, ~0.5 km deep) covered by bright material. The available data do not allow a conclusion to be reached on the local depths of this layer. The pit is traversed by dark lineaments which are possibly fractures, and seems to be surrounded by remnants of a central peak up to 0.5 km high. The morphology of Occator suggests that it is a relatively young crater, as the crater rim and walls appear rather sharp, and there are abundant terraces and landslide deposits. Very few superposed impact craters are observed on its rim, floor and ejecta. Occator partially formed on an east-southeast-trending fault, causing the rim scallop. Crater-based dating yields a relatively young crater age of ~78 Ma (Extended Data Fig. 3).

Feature A is located in the northwest part of an ancient 143-km-diameter crater (Fig. 2b, Extended Data Fig. 5) overlapped by a degraded 40.5-km-diameter crater. More specifically, the bright

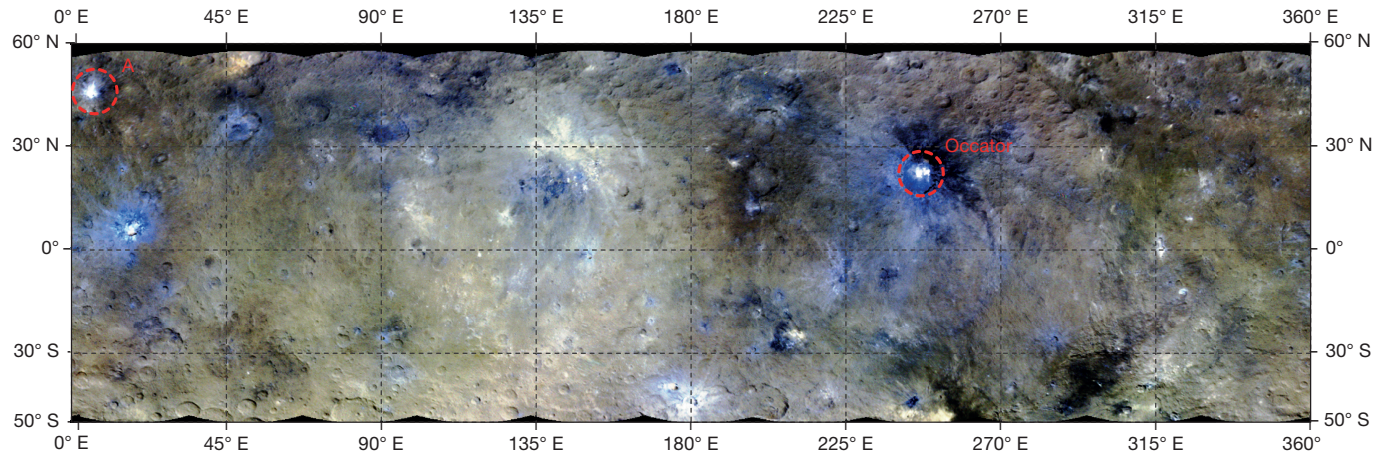

Figure 1 | Enhanced colour mosaic of the surface of Ceres. Data were obtained from 14,000 km distance and projected equirectangular in an RGB mosaic (colour coding of wavelengths: red R = 0.96 μm, green G = 0.75 μm, blue B = 0.44 μm). Red circles mark the location of the two brightest spots (Occator and feature A). Several dark patches, primarily associated with crater ejecta blankets, are also visible.

[1]Max Planck Institute for Solar System Research, Goettingen, Germany. [2]Planetary Science Institute, Tucson, Arizona, USA. [3]University of Winnipeg, Winnipeg, Canada. [4]Freie Universitaet Berlin, Berlin, Germany. [5]Technische Universitaet Clausthal, Clausthal-Zellerfeld, Germany. [6]University of California, Los Angeles (UCLA), Los Angeles, California, USA. [7]Johns Hopkins University, Laurel, Maryland, USA. [8]Royal Ontario Museum, Toronto, Canada. [9]TU Braunschweig, Braunschweig, Germany. [10]Brown University, Providence, Rhode Island, USA. [11]Jet Propulsion Laboratory, Pasadena, California, USA. [12]Lunar and Planetary Institute, Houston, Texas, USA. [13]Georgia Institute of Technology, Atlanta, Georgia, USA.

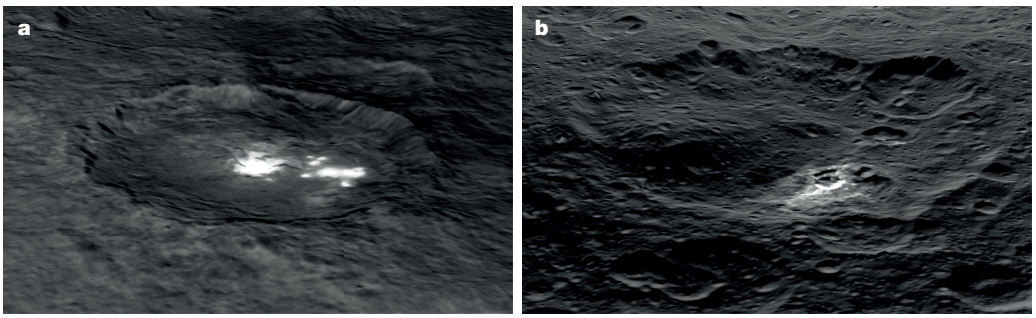

Figure 2 | Perspective views of brightest spots on Ceres. a, **b**, These spots are located on the floor of Occator crater at 19.4° N, 239.0° E (**a**) and at an unnamed crater at 41.7° N, 0.8° E (feature A; **b**). The clear filter images are wrapped onto topographic information derived from a stereo pair of images with elevation exaggerated three times (resolution ~0.4 km per pixel). The brightest spot on Ceres (**a**) is located in a depression on the floor of the ~90.5-km-diameter Occator crater. More than 10 smaller and fainter spots are found east of the central spot. The second brightest region on Ceres (**b**) is located in and around a 10-km-diameter crater (feature A).

material occurs inside a young, 10-km-diameter crater and nearby. Some spots located between 290° E and 360° E appear to be related to tectonic lineaments and/or large domes.

Because of the absence of strongly diagnostic absorption features in the wavelength range of the FC, any identification of specific phases must be considered tentative. We used absolute reflectance and the shape of the spectra to constrain the composition of the bright spots. These spots show not only substantially higher reflectances, but also a spectral shape that is different from the average for the whole of Ceres (see Fig. 3a, Extended Data Fig. 6). The spots exhibit a wavelength of maximum reflectance that is shifted from 0.65 μm (average surface) to 0.55 μm; also, the reflectance peak is more pronounced for the bright spots. It is important to note that the central part of the brightest Occator spot exhibits a spectrum that is different from the other bright spot spectra (Fig. 3b). Previous ground-based spectral observations of Ceres have suggested its surface to be similar to carbonaceous chondrite meteorites[14]. Observations by Dawn's Visible and Infrared Spectrometer have now revealed an average global surface that contains ammoniated phyllosilicates[15]. The absolute reflectance of the small-scale Occator bright spots coupled with the Herschel observatory's water vapour detection[4] suggests three possible candidate materials: water ice; iron-depleted clay minerals; and salts.

We conducted an extensive analysis of potential analogue materials. Of all materials considered, the centre of the brightest spot in Occator matches best with hexahydrite (six-hydrated magnesium sulfate, Fig. 3b). It is less consistent with other plausible minerals like smectites, although additional components that are spectrally featureless in this wavelength range, such as water ice, may also be present. Because of the detection of haze in the vicinity of the brightest spots (see below), a volatile component must be involved, which is likely to be water, as Herschel observations suggest[4]. With increasing distance from the centre of the Occator pit, the spectra become similar to those of the less bright spots on the surface, shifting the wavelength of maximum reflectivity from 0.65 μm to 0.55 μm, and increasing the negative spectral slope on the long-wavelength side of 0.55 μm. This spectral behaviour can be explained by a decreasing contribution from the brightest materials, and a possible change in their composition—to a less hydrated magnesium sulfate (kieserite, a mono-hydrated magnesium sulfate; Fig. 3c). Because of the lack of diagnostic spectral features in many candidate minerals, we stress that we cannot rule out other materials or processes, such as localized heating in contact with an ice-rich subsurface material that leads also to the formation of an iron-poor clay mineral, similar to processes on Mars[16,17].

In April 2015 the FC searched for plume activity; during this search, Ceres' limb was observed at high phase angles up to 155°. The goal was to detect potential dust particles in forward light scattering geometry. Although we did not detect any obvious plumes emanating from Ceres' lit limb, we observed near-surface haze in Occator that showed diurnal

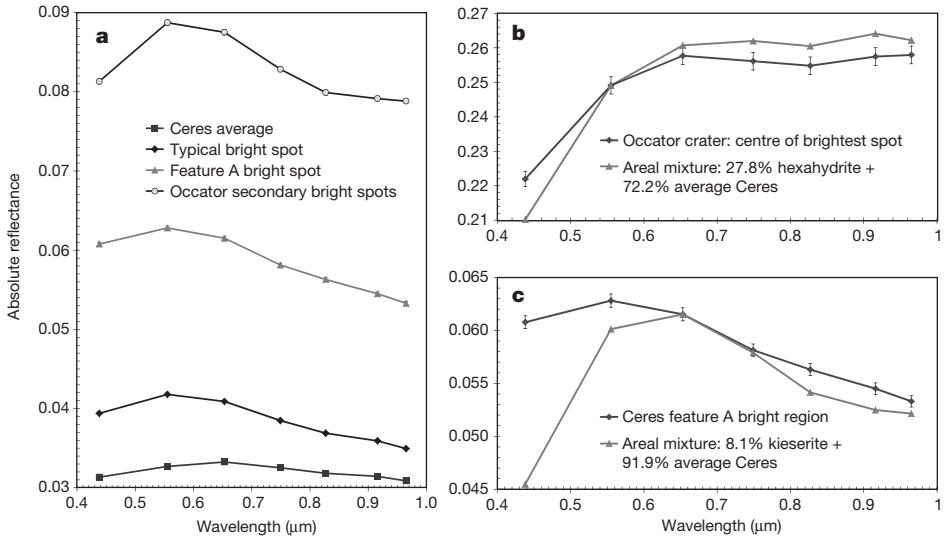

Figure 3 | Ceres colour spectra. a, Bright spot spectra peak around 0.55 μm and show negative spectral slopes on the long-wavelength side of 0.55 μm, whereas the average Ceres spectrum is darker and peaks around 0.65 μm. **b**, Spectrum of the centre of the brightest Occator spot compared with a numerical combination of an average Ceres spectrum plus a hexahydrite laboratory spectrum (see Methods section 'Spectral analysis'). **c**, Spectrum of feature A compared with a combination of an average Ceres spectrum and kieserite. The difference between the spectrum of feature A and this mixture at 0.44 μm is probably due to a difference in iron-bearing mineral content. Error bars, ±1 s.d.

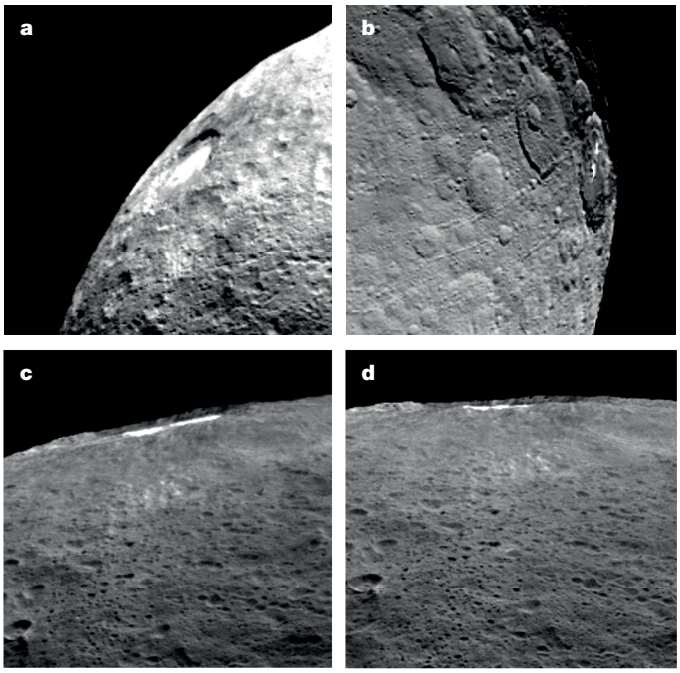

Figure 4 | Views of Occator crater at different times. Occator contains the brightest spot on Ceres. This is a pit covered by bright material, and the surrounding area shows a specific diurnal brightness rhythm, which becomes detectable at oblique views. **a**, Oblique view at noon reveals a diffuse near-surface haze (white) that fills the floor of its host crater. This haze disappears completely at dusk (**b**). The low column density of the haze is indicated by the very oblique limb views at noon (**c** and **d**), and the haze does not extend above the elevated southwestern part of the crater floor (left in **c**). There is a lapse of 450 s between the taking of the images shown in **c** and **d**.

variation, being pronounced at local noon and disappearing completely near dusk (see Fig. 4, Extended Data Fig. 7). Common among all four images displayed in Fig. 4 is an emission angle (angle between surface normal and line of sight) of 71°–87°, causing a high optical depth[18]. Despite the same range of optical depth at dusk, the absence of a detectable brightness excess at that time (Fig. 4b) proves the haze hypothesis. Any brighter solid material on the surface would remain at least partially visible at its phase angle of only 36°, which is even lower than that for the other three images (43°–70°).

Given the geographical correlation between Occator and a localized water vapour source detected by Herschel[4], we suggest that this haze layer consists of water-ice particles and dust. Similarly to the activity at the surface of a comet, the haze forms in the morning after sunrise by the sublimation of water. The stream of vapour lifts tiny particles of dust and residual ice. Despite Ceres' lack of a global internal heat source, this process resembles in part a mechanism suggested for vents on Enceladus[10]. We conclude that a similar process occurs at feature A (see Fig. 2b). The diurnal variation of haze on Ceres could also be responsible for the short time variability of the water vapour absorption measured by the Herschel telescope[4]. The presence of near-surface haze is realistic, because the measured outflow velocity of water on Ceres[4] is 0.3–0.7 km s^{-1}, comparable to the escape velocity[4] of ~0.52 km s^{-1}, which matches the expected speed for water molecules in this environment. As water sublimates it expands away from the surface, dragging along dust. Because of the speed distribution in the gas, a significant fraction will not leave Ceres, causing short-term haze and possibly proximal deposition. By assuming a system without internal forces and considering a water vapour loss of a few kilograms per second during daytime[4], the Occator spots are among the youngest features on Ceres. Our non-detection of plume activity and the low gas velocity rule out current cryovolcanic activity on larger scales, such as that seen on Enceladus[19]. Our observations are compatible with dusty ice material gently elevated away from surface deposits by sublimation, with no indication for other acceleration mechanisms. The process that has triggered this localized activity—for example, exposure of fresh ice by an impact or removal of a surficial cover by an internally driven explosive event[20–22]—remains unresolved.

Geophysical models suggest that Ceres contains about 25 wt% water in the form of ice and/or bound to minerals, evidenced by its low bulk density[1] of 2.2 g cm^{-3}. FC data are consistent with the presence of water ice on Ceres. Unlike the situation at active icy satellites[23,24], no high-reaching plumes are observed. However, it does seem that there is a significant amount of water ice[25], as also suggested by evolution models, potentially mixed with other phases, such as sulfates below a surface layer of insulating dark material. The global distribution and the geomorphology of the bright spots, showing lower reflectances than spots in Occator and feature A, but higher reflectances than the background surface, lead us to conclude that these are regions where the water sublimation process has stopped, probably owing to depletion of near-surface water ice resources or insulation by lag deposits. If most bright spots on Ceres represent these formerly active regions, then their global distribution indicates that the amount of near-surface water ice was (and maybe still is) significant, which is in agreement with the observation of relaxed crater morphologies on Ceres[25]. The global distribution of bright spots also suggests the presence of a global subsurface briny water ice layer. The simplest scenario is that the sublimation process of water ice starts after a mixture of ice and salt minerals is exposed by an impact, which penetrates the insulating dark upper crust. The horizontal extent of the near-surface, thin haze cloud corresponds to a zone in which the spectral shape changes from that shown in Fig. 3b (central pit) to those shown in Fig. 3a (outer pit). It reflects the distance-dependent trade-off between supply of ice and dust from the central pit and the final sublimation of the haze and deposition of residual dust.

Ceres is the first identified large body in the main asteroid belt showing not only primitive Solar System material, but also comet-like activity. Our results are consistent with widely distributed subsurface water or ice and water activity in the main asteroid belt, supporting the more recent view of a Solar System with a continuum in composition and ice content between asteroids and comets[26].

Online Content Methods, along with any additional Extended Data display items and Source Data, are available in the online version of the paper; references unique to these sections appear only in the online paper.

Received 3 August; accepted 21 September 2015.

1. Russell, C. T. & Raymond, C. A. (eds) *The Dawn Mission to Minor Planets 4 Vesta and 1 Ceres* (Springer, 2012).
2. McCord, T. B. & Sotin, C. Ceres: evolution and current state. *J. Geophys. Res.* **110,** E05009 (2005).
3. Castillo-Rogez, J. C. & McCord, T. B. Ceres' evolution and present state constrained by shape data. *Icarus* **205,** 443–459 (2010).
4. Küppers, M. *et al.* Localized sources of water vapour on the dwarf planet (1)Ceres. *Nature* **505,** 525–527 (2014).
5. Lebofsky, L. A., Feierberg, M. A., Tokunaga, A. T., Larson, H. P. & Johnson, J. R. The 1.7- to 4.2-micron spectrum of asteroid 1 Ceres: evidence for structural water in clay minerals. *Icarus* **48,** 453–459 (1981).
6. A'Hearn, M. F. & Feldman, P. D. Water vaporization on Ceres. *Icarus* **98,** 54–60 (1992).
7. Rivkin, A. S. *et al.* Hydrogen concentrations on C-class asteroids derived from remote sensing. *Meteorit. Planet. Sci.* **38,** 1383–1398 (2003).
8. Sierks, H. *et al.* in *The Dawn Mission to Minor Planets 4 Vesta and 1 Ceres* (eds Russell, C. T. & Raymond, C. A.) 263–327 (Springer, 2012).
9. Yamamoto, T. & Ashihara, O. Condensation of ice particles in the vicinity of a cometary nucleus. *Astron. Astrophys.* **152,** L17–L20 (1985).
10. Schmidt, J., Brilliantov, N., Spahn, F. & Kempf, S. Slow dust in Enceladus' plume from condensation and wall collision in tiger stripe fractures. *Nature* **451,** 685–688 (2008).
11. Martin, R. G. & Livio, M. On the evolution of the snow line in protoplanetary discs. *Mon. Not. R. Astron. Soc.* **425,** L6–L9 (2012).
12. Reddy, V. *et al.* Color and albedo heterogeneity of Vesta from Dawn. *Science* **336,** 700–704 (2012).
13. Nathues, A. *et al.* Detection of serpentine in exogenic carbonaceous chondrite material on Vesta from Dawn FC data. *Icarus* **239,** 222–237 (2014).

14. Vilas, F. & McFadden, L. A. CCD reflectance spectra of selected asteroids. *Icarus* **100,** 85–94 (1992).
15. De Sanctis, M. C. *et al.* Ammoniated phyllosilicates with a likely outer Solar System origin on (1) Ceres. *Nature* http://dx.doi.org/10.1038/nature16172 (this issue).
16. Milliken, R. E. & Mustard, J. F. Estimating the water content of hydrated minerals using reflectance spectroscopy: I. Effects of darkening agents and low-albedo materials. *Icarus* **189,** 550–573 (2007).
17. Ehlmann, B. L. *et al.* Geochemical consequences of widespread clay mineral formation in Mars' ancient crust. *Space Sci. Rev.* **174,** 329–364 (2013).
18. Blinn, J. F. Light reflection functions for simulation of clouds and dusty surfaces. *Comput. Graph.* **16,** 21–29 (1982).
19. Hansen, C. J. *et al.* Enceladus' water vapor plume. *Science* **311,** 1422–1425 (2006).
20. Cintala, M. J., Head, J. W. & Parmentier, M. E. Impact heating of H_2O ice targets: applications to outer planet satellites. *Lunar Planet. Sci.* **XI,** 140–142 (1980).
21. Bowling, T. J., Minton, D. A., Castillo-Rogez, J. C., Johnson, B. C. & Steckloff, J. K. Eroding the hydrosphere of 1 Ceres: water mass loss due to impact induced sublimation. In *Proc. Astrobiology Science Conf. 2015* abstr. 7478, http://www.hou.usra.edu/meetings/abscicon2015/pdf/7478.pdf (2015).
22. Williams, N. R., Bell, J. F. III, Christensen, P. R. & Farmer, J. D. Evidence for an explosive origin of central pit craters on Mars. *Icarus* **252,** 175–185 (2015).
23. Soderblom, L. A. *et al.* Triton's geyser-like plumes: discovery and basic characterization. *Science* **250,** 410–415 (1990).
24. Roth, L. *et al.* Transient water vapor at Europa's south pole. *Science* **343,** 171–174 (2014).
25. Schenk, P. *et al.* Impact craters on Ceres: evidence for water-ice mantle? In *European Planetary Science Congress 2015* Vol. 10, http://meetingorganizer.copernicus.org/EPSC2015/EPSC2015-400.pdf (2015).
26. Gounelle, M. The asteroid-comet continuum: in search of lost primitivity. *Geosci. World* **7,** 29–34 (2014).

Acknowledgements We thank the Dawn operations team for the development, cruise, orbital insertion and operations of the Dawn spacecraft at Ceres. We also thank the FC operations team, especially P. G. Gutierrez-Marques, I. Hall and I. Büttner. The FC project is financially supported by the Max Planck Society and the German Space Agency, DLR.

Author Contributions The respective observations were planned by the Dawn science-operations team involving A.N., M.H., M.S., C.A.R., C.T.R. and J.R. A.N., M.H., L.L.C., V.R., T.P., E.A.C., M.R.M.I., D.M.A., N.S. and T.K. contributed to the data analysis. The manuscript was written by A.N., M.H., M.S., L.L.C., V.R., T.P., E.A.C., N.S. and T.K. with reviews and updates by all authors.

Author Information Reprints and permissions information is available at www.nature.com/reprints. The authors declare no competing financial interests. Readers are welcome to comment on the online version of the paper. Correspondence and requests for materials should be addressed to A.N. (Nathues@mps.mpg.de).

METHODS

Crater-based dating of geological units. To determine an approximate formation age of Occator, we measured the crater size–frequency distribution observed on the continuous ejecta blanket to ~1 crater radius from the crater rim following the methodology described in ref. 27. The proximal portion of the ejecta blanket was excluded from the counting area, owing to its hummocky surface texture, to ensure reliable crater identification. The measurements were carried out in a GIS environment (ESRI's ArcGIS) using the CraterTools add-in[28], which helps to reduce map projection related distortions of crater diameters and counting areas. We used the FC clear filter images 40498, 40499, 40736, 40737, 40753, 40768, 40991 and 41006. The statistical analysis was performed using the CraterStats software[29] including verification for a spatially random distribution of the measured craters[30].

The cratering model age of 78 ± 5 Ma (that is, the formation age of Occator crater) derived for the ejecta blanket is based on the crater production and chronology functions of ref. 31. They assumed the same projectile distribution as observed on the Moon and a lunar-like time dependence of the projectile flux. These assumptions were also used for asteroid (4) Vesta, where measured crater retention ages are in good agreement with radiometric howardite–eucrite–diogenite (HED) meteorite ages[32].

We note that measured craters larger than 1.7 km in diameter are superposed by ejecta and, therefore, pre-date the Occator impact. In order to only utilize the smaller crater population superimposed on the ejecta, a resurfacing correction[30] was applied to derive the formation age. The crater size–frequency distribution is shown in a cumulative and differential plot (Extended Data Fig. 3).

Code availability. The software tools CraterTools[28] and Craterstats[29] used to measure and analyse crater size–frequency distributions can be downloaded free of charge at http://www.geo.fu-berlin.de/en/geol/fachrichtungen/planet/software/index.html. The Dawn FC images will be made available through the PDS website (https://pds.jpl.nasa.gov/).

Spectral analysis. We examined the as-measured bright spot spectra and the same spectra after subtraction of the average Ceres spectrum. After subtraction, the bright spot spectra retained their respective red and blue slopes, as well as differences in slope and 'kinks' in the spectra. We compared the salient spectral characteristics to a suite of plausible geological analogues (magnesium sulfates, magnesium carbonates, halide, water ice, hydroxides and clay minerals). Reflectance spectra from RELAB (http://www.planetary.brown.edu/relabdata/) and HOSERLab (http://psf.uwinnipeg.ca/FACILITIES/; http://psf.uwinnipeg.ca/Sample_Database/) and ref. 33 were convolved to FC band passes by averaging reflectance values in the laboratory spectra over the FC band passes[34].

The best matches to the Ceres bright spot spectra in terms of similar spectral shapes and presence of slope changes and kinks longward of 0.555 μm were used to generate areal mixtures involving the average Ceres spectrum. We assumed that this spectrum would be representative of the surrounding 'uncontaminated' materials. In the absence of optical constants for most of these materials, we chose to construct simple mathematical areal mixtures of the average Ceres spectrum with the best end member, matching the spectra at the 0.653 μm FC band pass and weighting each spectrum by an abundance factor. Although mathematical areal mixtures are not ideally representative of how the bright materials are present on Ceres, they do provide a lower limit on the abundance of the bright materials, as bright materials are darkened by opaque phases (such as average Ceres) more in intimate versus areal mixtures. In our spectral comparisons, we focused on using fine-grained (<45 μm) reflectance spectra of bright materials and used only binary mixtures.

Sample size. No statistical methods were used to predetermine sample size.

27. Platz, T., Michael, G. G., Tanaka, K. L., Skinner, J. A. Jr & Fortezzo, C. M. Crater-based dating of geological units on Mars: methods and application for the new global geological map. *Icarus* **225,** 806–827 (2013).
28. Kneissl, T., van Gasselt, S. & Neukum, G. Map-projection-independent crater size-frequency determination in GIS environments — new software tool for ArcGIS. *Planet. Space Sci.* **59,** 1243–1254 (2011).
29. Michael, G. G. & Neukum, G. Planetary surface dating from crater size–frequency distribution measurements: partial resurfacing events and statistical age uncertainty. *Earth Planet. Sci. Lett.* **294,** 223–229 (2010).
30. Michael, G. G., Platz, T., Kneissl, T. & Schmedemann, N. Planetary surface dating from crater size–frequency distribution measurements: spatial randomness and clustering. *Icarus* **218,** 169–177 (2012).
31. Schmedemann, N. *et al.* A preliminary chronology for Ceres. In *Lunar Planet. Sci. Conf. 46* abstr. 1418, http://www.hou.usra.edu/meetings/lpsc2015/pdf/1418.pdf (2015).
32. Schmedemann, N. *et al.* The cratering record, chronology and surface ages of (4) Vesta in comparison to smaller asteroids and the ages of HED meteorites. *Planet. Space Sci.* **103,** 104–130 (2014).
33. Bishop, J. L. *et al.* Spectral properties of Na, Ca-, Mg- and Fe-chlorides and analyses of hydrohalite-bearing samples from Axel Heiberg Island. In *Lunar Planet. Sci. Conf. 45* abstr. 2145, http://www.hou.usra.edu/meetings/lpsc2014/pdf/2145.pdf (2014).
34. Sierks, H. *et al.* The Dawn Framing Camera. *Space Sci. Rev.* **163,** 263–327 (2011).
35. Reddy, V. *et al.* Photometric properties of Ceres from telescopic observations using Dawn Framing Camera color filters. In *Lunar Planet. Sci. Conf.* 46 abstr. 1663, http://www.hou.usra.edu/meetings/lpsc2015/pdf/1663.pdf (2015).

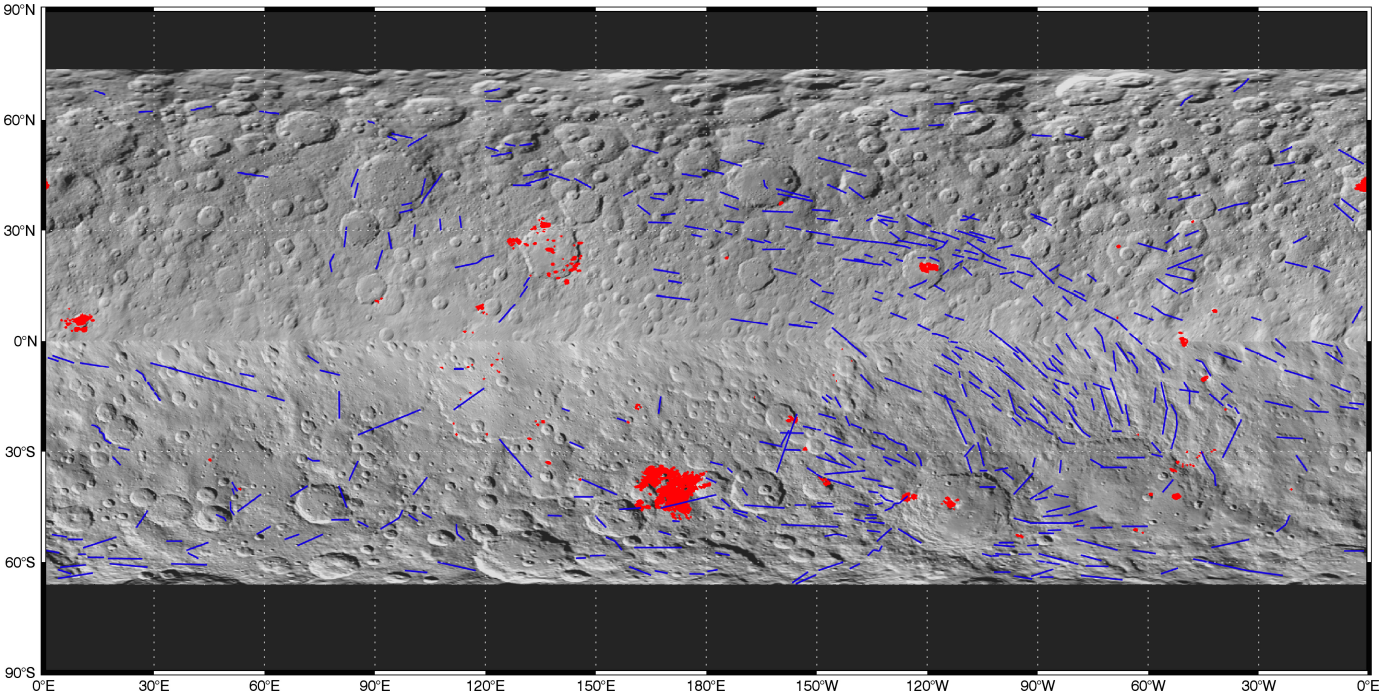

Extended Data Figure 1 | Clear filter mosaic and locations of bright material (red) and global lineaments (blue). Background map of Ceres is shown in equirectangular projection, combining FC clear filter mosaics from two different sequences of observations during the Rotational Characterization 3 phase at a distance of ~14,000 km (RC3). Several mosaics (all sequences from RC3 phase) with different stretches have been used for the mapping of the linear features. Both fractures and alignment of circular features have been mapped in blue. The former features could correspond to faults, and the latter could be pit crater chains or secondary crater chains. Bright material surfaces are those showing an absolute reflectance larger than 0.037 at 0.55 μm.

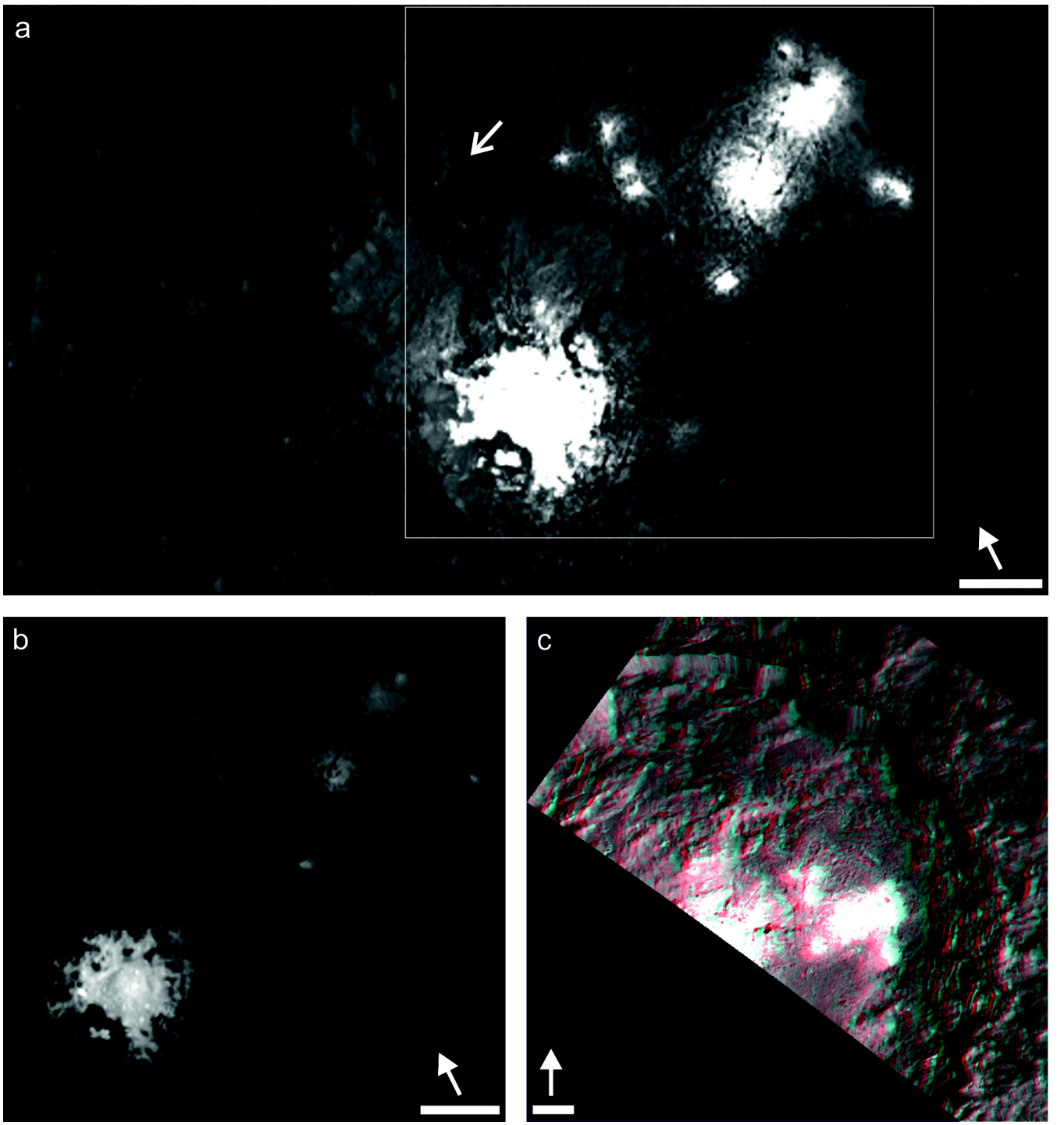

Extended Data Figure 2 | Interior of Occator crater. a, Image shows a scene of the centre of Occator crater from High Altitude Mapping Orbit (FC image 40752, resolution ~140 m per pixel) revealing curvilinear depressions and a smooth pond-like feature (arrow at upper centre) at one of its ends. A possible explanation of the last feature is former short-term liquid-flow material. **b**, Central and peripheral bright spots within Occator crater. A nonlinear stretch is applied to enhance the interior structure of the bright spot. **c**, 3D anaglyph (red–cyan glasses are required to see this scene in 3D) showing the northeastern portion of Occator crater. A flow lobe with well-defined margins at the image's centre is clearly visible. Note that the extent of secondary bright spot occurrences is confined to the extent of the flow lobe. Extensive slumping of wall material is observed in the northern portion of the crater. The anaglyph (images 40736 and 40752) has a vertical exaggeration of 1.9 if viewed at a distance of 50 cm. Arrows above scale bars point towards north; scale bars are 7 km long.

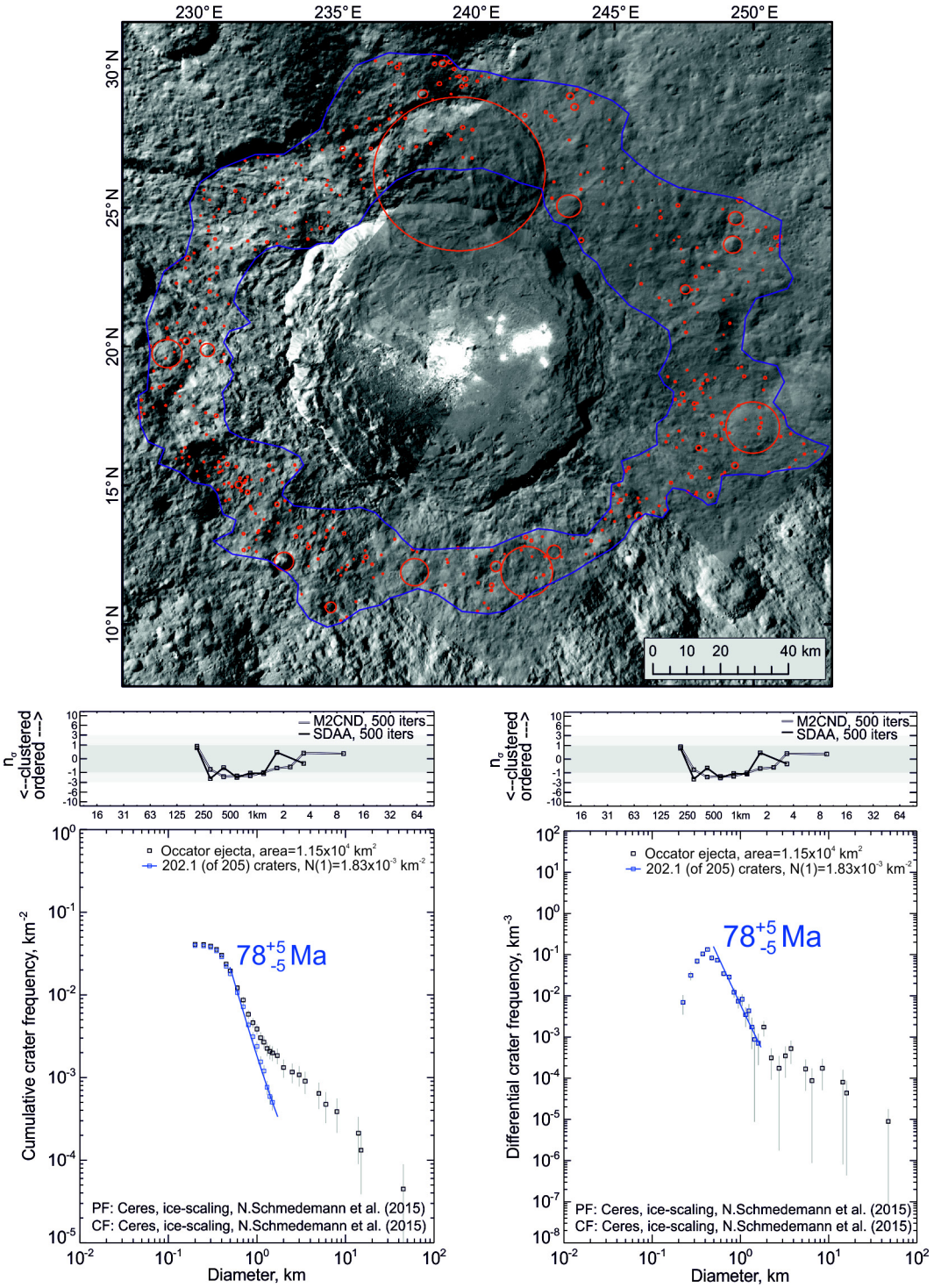

Extended Data Figure 3 | Crater counting area, superposed impact craters and model age. The upper panel shows the crater counting area (blue outline) and measured impact craters (red outlines) on the ejecta blanket of Occator crater (FC images 40498, 40499, 40736, 40737, 40753, 40768, 40991 and 41006). On the basis of the mapped crater size–frequency distribution, we derived a model age of 78 ± 5 Ma for the formation of Occator crater (lower panels) shown in cumulative (left) and differential (right) plots. To model an absolute age we used the production function (PF) and chronology function (CF) of ref. 31 and fitted the isochron to the crater diameter range 0.5–1.7 km. Error bars are $\pm$ the square-root of the cumulative number of craters per bin divided by the counting area—the largest bins contain fewer craters and therefore have the largest error bars. The reference value N(1) denotes the cumulative number of craters larger than 1 km in diameter per square kilometre. Upper insets show results from a Monte-Carlo-based randomness analysis for the measured crater population using the mean second-closest neighbour distance ('M2CND') and the standard deviation of adjacent area ('SDAA') methods[30]. Standard deviations n_σ are plotted above and below the Monte-Carlo-derived mean. Details about the methods are given in ref. 30. Here, the observed crater population plots within the 3σ range indicating a random distribution.

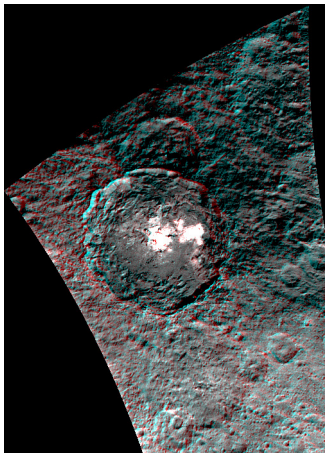

Extended Data Figure 4 | 3D anaglyph of Occator crater. The interior of the 90.5-km-diameter crater is characterized by an abundance of terraces and a smooth inner floor surface. The inner crater rim appears scalloped in places. The central pit with the brightest spot on Ceres is partially rimmed. Occator ejecta extend up to one crater diameter outwards, partially or completely burying pre-existing terrain and impact craters. The anaglyph is composed of FC images 37674 and 37666. Vertical exaggeration is approximately 4.5 if viewed at a distance of 50 cm.

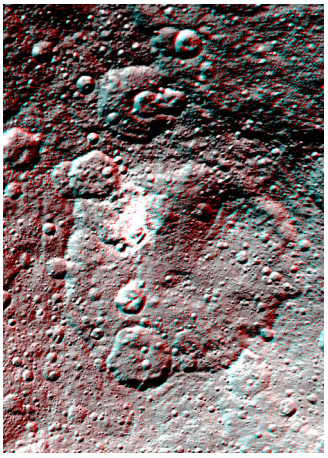

Extended Data Figure 5 | 3D anaglyph of an unnamed crater hosting feature A. The large crater accommodating feature A is degraded and marked by a low-relief crater rim partially eroded by subsequent impact craters. Its interior exhibits a densely cratered floor and hosts an asymmetric dome. The bright material is exposed within a 10-km-diameter crater on the wall of the larger, degraded crater and its vicinity. 3D anaglyph is composed of FC images 38409 and 38407. Vertical exaggeration is approximately 3.0 if viewed at a distance of 50 cm.

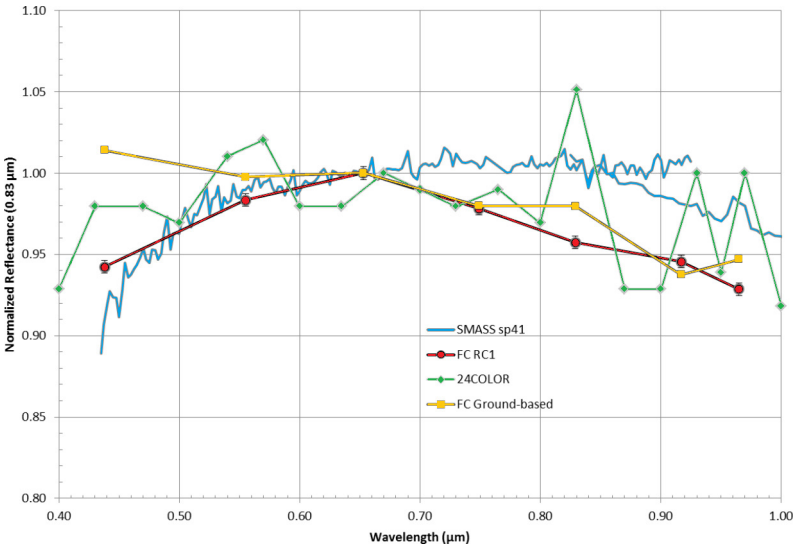

Extended Data Figure 6 | Average FC colour spectrum ('FC RC1') of Ceres and ground-based spectra. Ground-based spectra ('SMASS sp41', '24COLOR' and 'FC Ground-based') of Ceres are presented for comparison. Ceres spectra, obtained by ground-based telescopes, in general show a large variety. The ground-based average colour spectrum of Ceres using FC spare filters[35] is, except for filter 0.44 µm, in good agreement with the in-flight spectrum. We note that the ground-based spectra are obtained under different viewing geometries and are not photometrically corrected compared to the in-flight data. Ground-based spectra 'SMASS sp41' and '24COLOR' are available at http://sbn.psi.edu/pds/archive/asteroids.html. Spectrum 'FC Ground-based' is presented in ref. 35.

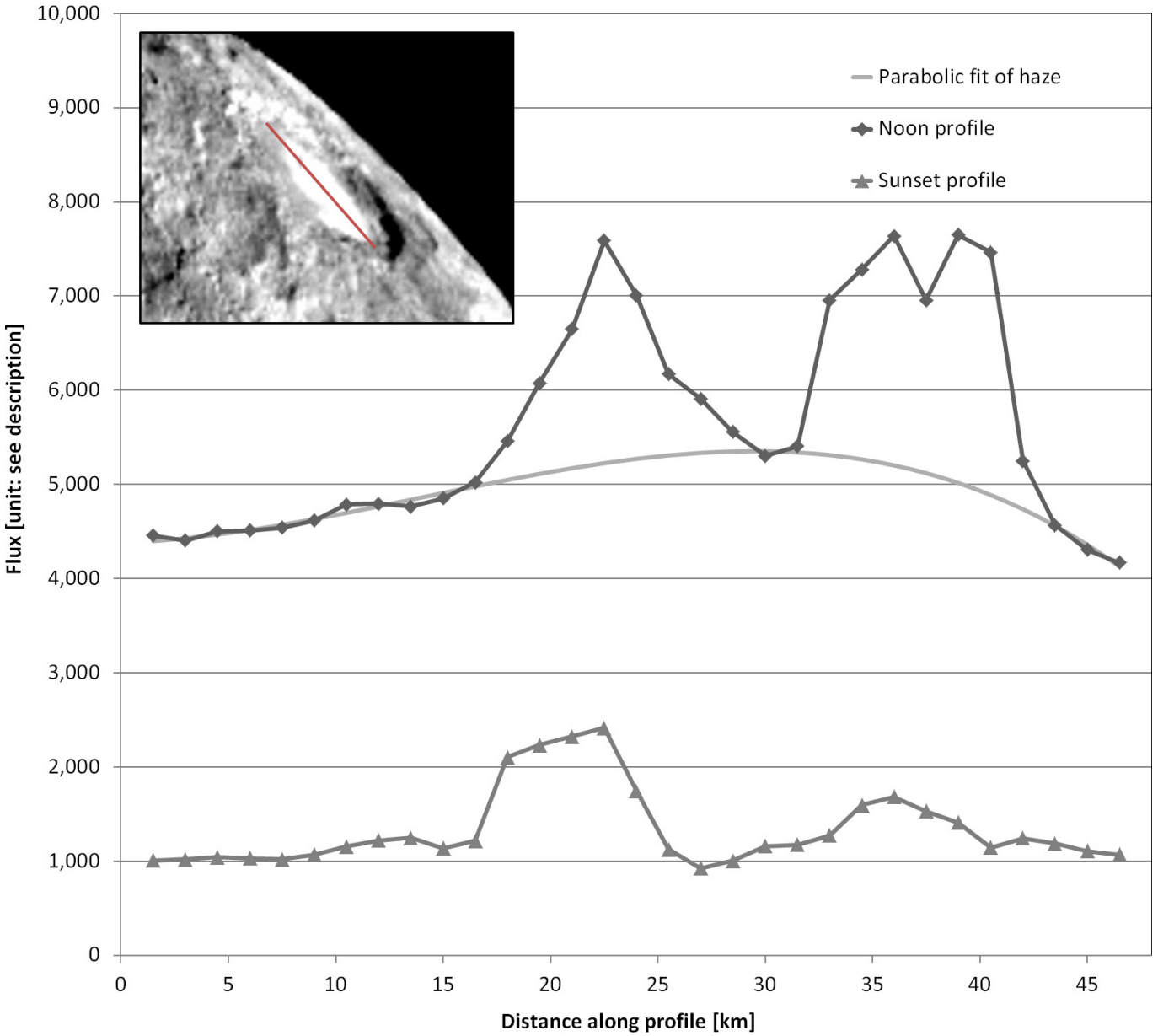

Extended Data Figure 7 | Haze cloud intensity profile. Two flux profiles from FC clear filter images across the central part of Occator crater (indicated by the red line; see inset). Units of flux are counts per pixel (~1.5 km × 1.5 km). Each profile crosses the centres of the brightest and second brightest spots (see inset, noon image 37113). Two images were selected, the first (37113) showing the scene at low incidence and high emission angles, that is, an oblique view near local noon ('Noon profile'). The second image (36681) was obtained at high angles in both emission and incidence, showing an oblique view near local sunset ('Sunset profile'). While the 'Noon profile' shows a signal enhancement centred between the peaks, the 'Sunset profile' does not show this. The enhancement is best described by a parabolic fit of the background, ignoring the signal peaks ('Parabolic fit of haze'). The shape of this fit is consistent with a diffuse light scattering component in Occator crater at maximum insolation, observable at very oblique views, which increase the length of the light path through the layer, resembling the phenomena associated with a haze layer.